Proceedings of ASME Turbo Expo 2022
Turbomachinery Technical Conference and Exposition
GT2022
June 13-17, 2022, Rotterdam, The Netherlands

GT2022-82538

THERMAL MANAGEMENT FOR ELECTRIFICATION IN AIRCRAFT ENGINES: OPTIMIZATION OF COOLANT SYSTEM

N. Raske[1], O. Ausin Gonzalez[2], S. Furino[1], M. Pietropaoli[1], S. Shahpar[2], F. Montomoli[1]

[1]ToffeeAM, London, UK
[2]Innovation Hub-Future Methods, Rolls Royce plc, Derby, UK

ABSTRACT

This work shows the application of fluid Topology Optimization for the thermal management of electric parts in aircraft engines. There is a growing trend in electrification of current engines, but this requires higher power to be dissipated. Standard coolant systems based on serpentines are not effective enough to remove the heat produced by these systems. In this work a new solution is shown which has a higher heat dissipation, lower pressure loss and a reduction in the mass of the heat exchanger. The optimization is carried out with the commercial solver TOffee. Manufacturing constraints allow the part to be manufacturable using two different methods: additive manufacturing and milling with diffusion bonding.

Overall, the optimized geometry, a nearly 2D cold plate with extruded channels, shows higher heat dissipation and a weight reduction of 38.5% if compared with the baseline heat exchanger. The overall pressure drop has been also reduced by 65%.

Keywords: Fluid Topology Optimization, Conjugate Heat Transfer

NOMENCLATURE

α	Fluid Resistance	$kg/m^3 \cdot s$
ρ	Density	kg/m^3
c	Specific Heat Capacity	$J/K \cdot kg$
CHT	Conjugate Heat Transfer	
F, F_1, F_2	Objective Function and Components	J
k	Thermal Conductivity	$W/m \cdot K$
$\boldsymbol{n}$	Surface Normal	$[-]$
p	Pressure	Pa
$\boldsymbol{u}$	Velocity vector	m/s
w	Weighting	$[-]$
μ	Dynamic Viscosity	$kg/m \cdot s$

INTRODUCTION

There is a growing interest in electrification of aircraft engines [1] with a trend towards a 100% electric aircraft for short to medium haul flights. The growing amount of electric power delivered needs more efficient thermal management systems, both for conventional gas turbines and for electric engines. There is a need for optimization techniques to improve thermal management of the battery pack, motor, and electrical components such as inverters, solid-state switches, and micro-electronic devices [2]. The thermal requirements of these components change the optimal aircraft trajectory [3], imposing temperature limits that constrain performance. In particular, the heat exchanger area increases or can increase with the specified climb rate.

Designing heat exchange devices for the next generation of conventional gas turbines (with increased electrical parts) and electric aircraft engines will be critical to ensure efficient, reliable, and safe performance [4, 5]. Heat sources in a single aircraft will range from high power battery packs to low power microelectronic components. In both scenarios heat must be transferred from a solid heat source and into a transport fluid. This is often managed by a so-called cold plate device. The traditional configuration constitutes a pipe, or series of pipes, strategically arranged in a serpentine pattern that traces the heated region to enhance heat transfer. Different methods have been developed to improve the thermal performance of heat exchangers including modified surface roughness of the pipes, micro-channel, surface area and turbulence promoters, cellular materials, heat pipes, and so on [6, 7]. The key idea is to increase the fluid mixing induced by the surfaces to increase the heat transfer rate. The resulting problem therefore balances heat exchange between the solid and fluid with the pressure loss incurred by forcing fluid through the device [8, 9, 10]. These are often two conflicting objectives that an efficient device will strike a balance in-between. The traditional design of serpentine paths for cold plates have only a few parameters which can be modified to achieve this balance. The traditional configuration uses a combination of straight ducts and U-bends. Shape optimization of the serpentine has been shown to improve heat transfer, however local heat transfer can be more effectively improved with rib arrangements [11]. The serpentine passage generates large flow separation and vortices, which improve mixing and therefore convective heat transfer, with the drawback of a large pressure drop at each turn. Other factors to consider for the design of serpentine passages are the number of channels or the direction of the tubes in relation to the heat sources, where cooling efficiency is rarely enhanced when more than five channels are used, but the temperature uniformity is improved [12]. Mangrulkar et al. [13] performed a review of recent developments for improving thermal performance of cross-flow heat exchangers, noting that guidelines for heat exchanger design should include the relative importance of convective versus conductive heat transfer (i.e. the Nusselt number) and the pressure loss across the device. This bears out in analytic studies where increase in surface area increases the conductive heat flux but reduces the convective contributions [14].

Fluid topology optimization is an ideal tool for addressing the conflicting cold plate design requirements and has already been developed for fluid heat exchange applications [15, 16, 17]. Topology optimization is a design method which frames the domain (design space) and environment (loads, energy, etc.) mathematically and optimally distributes mass to best satisfy the objective function subject to some defined constraints. The method has been used to reduce the mass of aircraft structural components [18, 19], design meta-materials comprised of periodic lattice structures [20], and develop novel heat exchangers [21]. There have been a number of studies using shape optimization techniques to improve the location and shape of the cooling channels [22, 23]. However, these do not fundamentally change the design. Fluid topology optimization can be used to create radically different flow paths than traditional serpentine designs that improve heat transfer properties, reduce pressure losses, and reduce the mass.

Additive manufacturing can produce intricate structures at a complexity that is not possible for subtractive techniques. In the aerospace field this has translated into designs that reduce mass, lead times and costs [24]. Powder bed fusion uses high power lasers or electron beams to sequentially melt and fuse layers of metal powder. It can reliably produce structures on the micro scale which has enabled thin lattice structures and lattice members to replace traditional solid features. This has advanced the state of the art for structural [24] and heat exchange applications [25]. Combining the growing capabilities of additive manufacturing [26] means that cold plate designs can now take advantage of the greater degrees of freedom offered by optimization techniques.

Predicting the performance of a cold plate requires models for how the solid and fluid components interact to transfer heat. This is typically done with a Conjugate Heat Transfer (CHT) model where the solid and fluid domains are meshed separately but share a common temperature or heat flux interface. Conjugate heat transfer is used for fluid dynamic problems where energy is transferred between a solid and a fluid domain. In practice, this means that the CFD solver simultaneously solves the Navier-Stokes equations in the fluid and heat conduction in the solid region. It does so by creating an interface coupled wall where the two zones are in contact. Instabilities could occur at that interface if the meshing is not done in a consistent manner.

CHT has been used to predict the temperature distributions and pressure losses for serpentine structures [27]. It also has usages across a wide range of heat exchanger problems, including chemical practices to mimic artificial exothermal reactions in ceramic open-cell foams [28] and thermal-hydraulic systems for nuclear applications [29]. Papukchiev et al. [29] compared the CFD solutions using ANSYS CFX for a Generator reactor system for a fluid only simulation to those from a CHT simulation. Despite the increased number of elements in the simulation, it was concluded that CHT was necessary to capture the coupled effects of fluid-solid heat transfer. This method was also considered in the analysis and heat transfer enhancement for a serrated finned tube. It was used to predict the temperature distribution for the shell and tube geometry and the pressure drop through the fluid domain, managing to find increased results on the heat transfer by 3.53% to 5.14%.

In this work a cold plate design for the thermal management of a model electric system is analyzed. The power output is 1.2kW and is representative of a small to moderate power system, a group of thyristors or other solid-state semiconductor devices. A cold plate with a serpentine channel is adopted as a representative baseline cooling strategy because it is a common approach for cold plate design. An innovative design is obtained via fluid Topology Optimization with the commercial solver TOffee.

For this study, the Optimized and Datum geometries were analyzed as a CHT problem where separate meshes were generated for the fluid and solid components and were coupled for the solution process.

1. METHODS

This study contrives a generic heating scenario where a cooling plate is surrounded by heat sources, see Figure 1. It is spatially confined to a narrow region where the fluid is returned on the same side as it enters. This forms the cooling region and is the design space for the present study. The cooling region is bounded by heat spreading plates which are assumed to be constructed from aluminum.

Any members or pipes placed inside the cooling region are also constructed from aluminum and considered to be perfectly bonded to the heat spreaders, i.e. there is no thermal discontinuity between solid components. Inside both heat spreaders are three heat sources producing 400W of power each.

Two designs are compared, a traditional serpentine pipe and a fluid topology optimized design. The cases are comparable in that they are both operating with a constant coolant flow rate of 3 l/min, are surrounded by heat sources of the same size and power and have the same thickness. The inlet and outlet sizes are different but have the same location. This means that the inlet

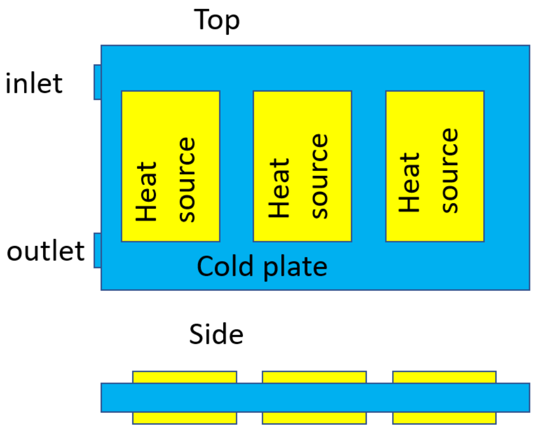

FIGURE 1: Sketch of the fluid region, blue, and heat sources, yellow, for the generic test case.

velocity for the serpentine case is higher than that of the empty design space used for the optimized case. This discrepancy was included to give design freedom to the optimizer. It is possible for the optimization software to constrict flow, increasing velocity, but it is not possible for it to expand beyond the domain. The materials properties for the solid and fluid components are described in Table 1 while the operating parameters are described in Table 2.

The outer dimensions of the cold plate are 228 mm of length, 130 mm of width and 12 mm of thickness. The coolant used in this exercise is a mix of 40% water and 60% ethylene-glycol at a flow rate of 3 liters per minute. The heat sources attached to the plate are also identical and equally spaced, being three at the top and three at the bottom.

TABLE 1: Material properties for the solid and coolant.

	$\rho\left(\frac{kg}{m^3}\right)$	$C_p\left(\frac{J}{K\cdot kg}\right)$	$\mu\left(\frac{kg}{m\cdot s}\right)$	$k\left(\frac{W}{m\cdot K}\right)$
40%Water + 60%Ethylene-Glycol	1068	3424	1.65e-3	0.4
Aluminum Alloy	2719	871	-	202.4

TABLE 2: Cold plate operating parameters.

Flow Rate $\left(\frac{m^3}{s}\right)$	Inlet Pressure (Pa)	Inlet Temperature (K)	Power (W)
0.3e-3	$\nabla p = 0$	333	400

Each design was analyzed as a conjugate heat transfer (CHT) problem where separate meshes were generated for the fluid and solid component and were coupled for the solution process. The energy equation was solved on the solid domain while in the fluid domain the Navier-Stokes equations were solved using the Pressure-Based SIMPLE Coupled algorithm [30] with additional coupling for transport of thermal energy. This was implemented using the commercially available ANSYS Fluent v19.0 software [31]. Due to the small dimensionality of the flow channels, particularly in the optimized design (shown in subsequent sections), the Reynolds number is low and some flow separations are expected therefore the SST k-ω turbulence model was applied to the fluid domains.

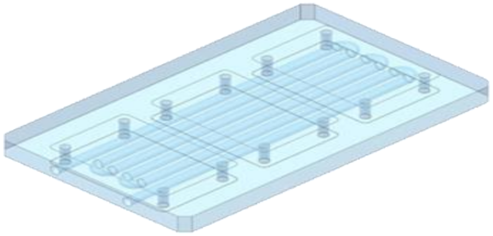

FIGURE 2: Schematic of the fluid region for serpentine case. The rods which fix the heat sources to the plate are neglected in the study.

2.1 The Serpentine Cold Plate

The serpentine test case, shown in Figure 2, represents a common engineering design for a cold plate. It is comprised primarily of an aluminum casing with an embedded serpentine channel. The channel configuration is established using a series of five U-Bends connected through six equally spaced cylindrical tubes with a 3 mm radius. The passage is designed so the cooling fluid only flows between the top and bottom heat sources, reaching the opposite end of the plate.

2.2 Assessment of CFD accuracy

A high-fidelity CHT Computational Fluid Dynamic (CFD) study has been conducted to ensure accuracy of results. This method has been implemented in the study of the heat transfer performance of the serpentine passage to obtain a reliable datum. A CFD analysis using the same solver was then performed on the optimized topology, after the geometry has been exported and meshed, to obtain the heat transfer performance of the new cold plate. This technique serves to compare both cold plates, the original and optimized, and to quantify the effectiveness of the optimization method.

Two different types of CFD meshes were compared: a quad-tree Cartesian type mesh and an unstructured tetrahedral mesh. Both meshes are shown in Figure 3 The first meshing tool, BOXER, was created by Cambridge Flow Solutions [32] and the second, ICEM, was developed by ANSYS. The BOXER is Hex rich and uses local refinement around the heat cells and the fluid tube to better capture the thermal exchange between the fluid and the solid zones. For the ICEM mesh, the solid region used a hexa-core while the fluid volume region used tetrahedral cells. To ensure that the inlet and outlet boundaries had enough cells to represent the fluid physics, a maximum cell length of 0.5 mm was applied consistently in all the ICEM meshes. It can be seen in Figures 4 and 5 a comparison of the top and entry wall surfaces between both types of meshes having a similar total cell count of 5M elements.

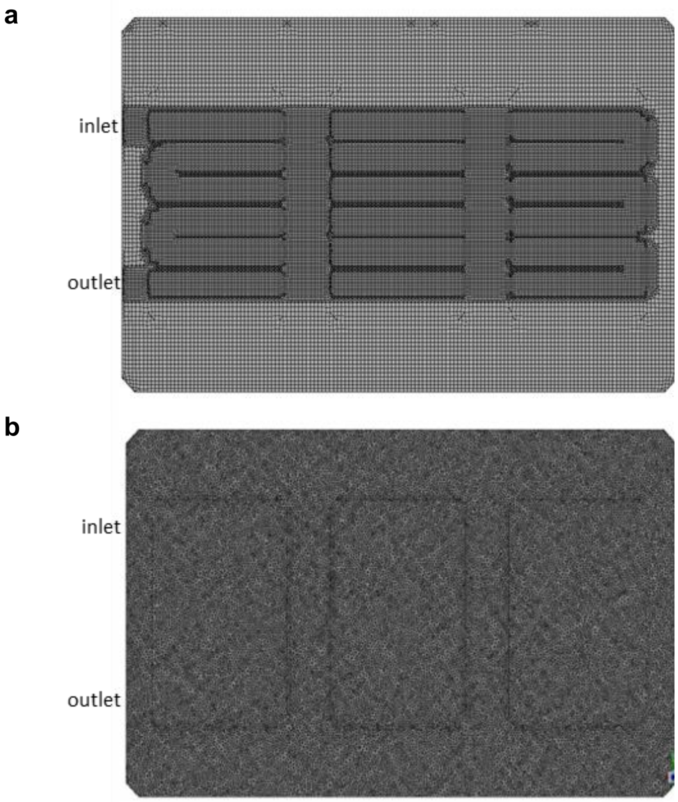

FIGURE 3: (a) BOXER hexahedral surface wall mesh and (b) ICEM tetrahedral surface wall mesh.

Both meshing techniques use the Oct-Tree type method. The computational domain is firstly divided in hexahedral cells. In ICEM, these are converted into tetrahedral cells, with the advantage of simplifying the 3D mathematical model and offering smoothing around neighboring cells. The BOXER technique projects the hex-dominant volume cells towards the surface of the geometry to generate the final body-fitted mesh. The Cartesian mesh is desired for a uniform mesh distribution along smooth surfaces but do not capture the curvature of the volume appropriately, that is why extra refinement was created around the areas of interest.

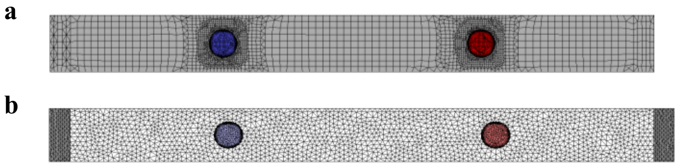

FIGURE 4: (a) BOXER hexahedral entry wall mesh and (b) ICEM tetrahedral entry wall mesh. In both cases the blue corresponds to the inlet and the red corresponds to the outlet, both of which are labelled in Figure 3.

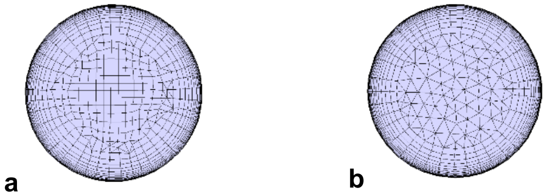

FIGURE 5: (a) BOXER hexahedral entry wall mesh and (b) ICEM tetrahedral entry wall mesh. Both cases are taken from the inlet shown in blue in Figure 4 and at the location shown in Figure 3.

The complexity of the conjugate heat transfer problem resides in the boundary where the fluid and solid zones are in contact. For this reason, this problem requires a high mesh resolution in the boundary layer of the fluid zone. A prism layer was added for that purpose for both meshes with the same characteristics: first height of 2E-6 m and 20 layers. For the tetrahedral mesh, quadrilateral faces are created automatically when the prism layer is activated. In the Cartesian mesh, the prismatic layers are added after the mesh is morphed to the surface. The profile at the inlet showing the prism layer for both meshes can be seen in Figure 5.

One of the main differences between these two types of mesh for convective heat transfer applications is the volume away from the walls, where the bulk of fluid is transported. The non-uniform tetrahedral mesh can lead to numerical errors that behave like diffusion, producing artificial dissipation. This issue has been mitigated near the walls by applying a prism layer inside the fluid domain. Close to the boundary, the stream-wise change is much smaller than the cross-stream change, which means that the mesh does not need much refinement in the flow direction. The hex-mesh is then appropriate for this application.

To conduct a mesh independence study, five meshes with different seed sizes were created for each type. The total number of elements in each mesh was roughly matched to conduct the comparison, rather than the cell size (since the size of the elements is non-uniform within the same mesh). Figure 6 shows the total cell count of the BOXER and ICEM mesh for the five meshes used here. Mesh 1 has the smallest number of elements, roughly 1 M, Mesh 2 ~ 2M, Mesh 3 ~ 5 M, Mesh 4 ~ 10 M and Mesh 5 ~ 20 M.

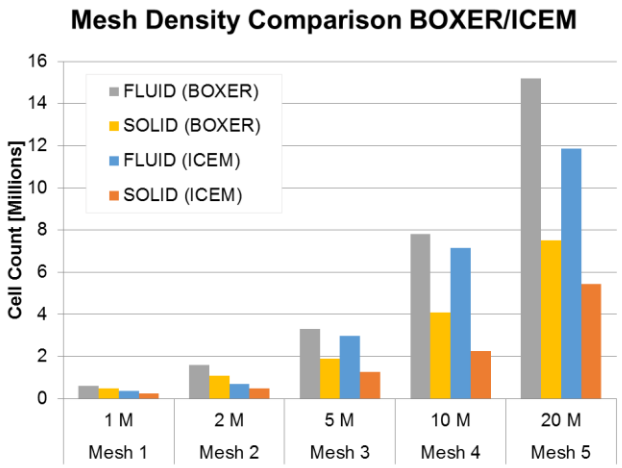

FIGURE 6: Mesh Density Comparison BOXER/ICEM mesh.

Turbulent flows are affected at the boundary layer where the effects of viscosity are significant. One way of ensuring that the mesh cell size is appropriate for capturing the fluid physics near the wall, is by checking the y+ parameter during the CFD simulations. This non-dimensional value represents the distance from the wall to the first mesh node. For the turbulence model chosen here (k-ω), it should be close to 1 or less. The prism layer in the ICEM case was modelled identically for the five meshes, they all presented a maximum y+ value of 0.28, while the BOXER meshes decreased from ~ 1.21 to 0.29 as the total cell count increased from 1 to 20 million.

The conjugate heat transfer problem was computed using the commercially available ANSYS Fluent v19.0 software. The energy equation was enabled, accounts for viscous heating, and uses a k-ω SST turbulence model. The problem was solved by appending two independent meshes for the solid and fluid regions. At the interface the fluid and solid equations are coupled through temperature and hydrostatic stresses. A pressure-velocity solver was used with an implicit coupled scheme and a Courant-Friedrichs-Lewy stability condition of 2, as it brought both the energy (solid and fluid) and fluid continuity, momentum and turbulence residuals to an error of at least 1E-4, ensuring that the results were fully converged. The simulations were run over 15000 iterations in parallel using 4 CPU processors.

Several key parameters were identified to evaluate this problem: the fluid pressure drop between the inlet and outlet (Figure 7b), the minimum, maximum and average temperature on the wall (Figure 7a) and the surface heat patches. Monitoring the pressure drop and surface temperature served as an indication to identify which functions of the conjugate heat transfer problem, Navier-Stokes fluid equations or energy transport equations converged, and how to modify the simulation setting if they failed.

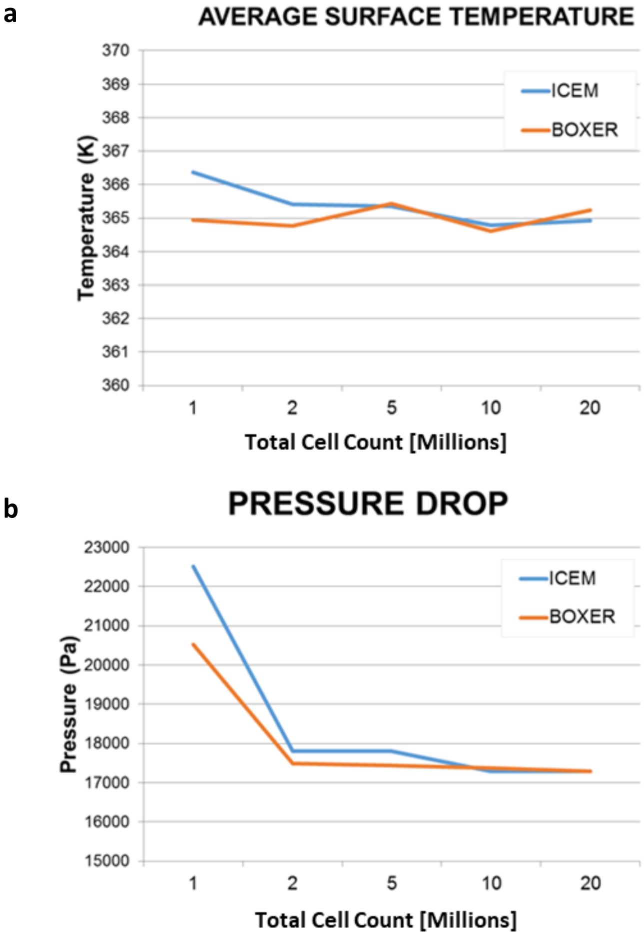

FIGURE 7: ICEM and BOXER average surface temperature (a) and fluid Pressure Drop from inlet to outlet (b).

The graphs from Figure 7 shows how the ICEM meshing technique tends to estimate higher pressure and temperature values than the BOXER mesh for the coarser mesh densities. As the number of cells rises, both cases have a similar performance; pressure drop stabilizes at around 17300 Pa, and the average surface temperature at the plate's wall slightly oscillates around 365 K. The difficulty of solving CHT problems can be seen in the divergence of results between 1M and 2 M elements. Figure 7 shows that the BOXER mesh reaches stability faster than the ICEM mesh, after 2 M cells are used. The surface temperature plots (Figure 7a) combines the minimum surface temperature (blue) with the temperature gradient (orange) adding together the maximum temperature found at that surface. It is noticeable that for both meshing techniques, regardless of the cell count, the minimum temperature is stable at 350 K – only the 5 M BOXER mesh gives a peak of 353 K. The maximum temperature shows to be converged at 372 K for most of the results.

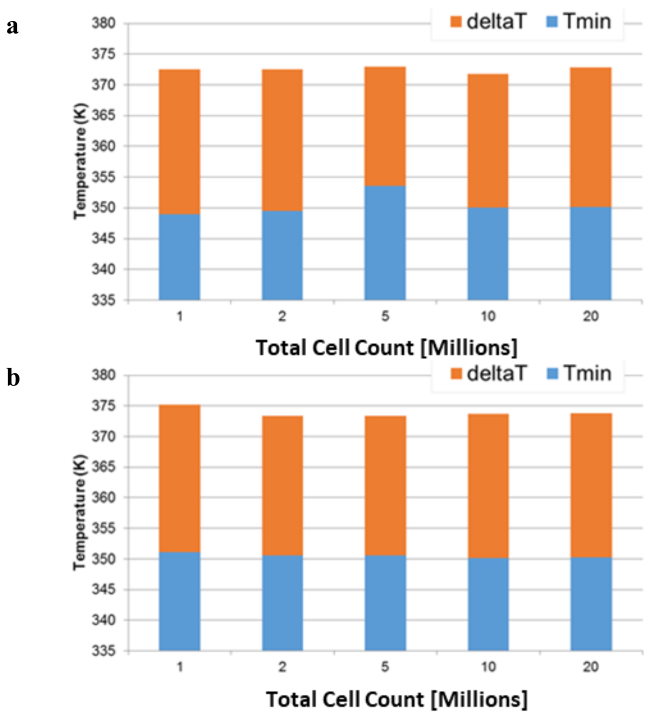

FIGURE 8: Surface temperature (minimum + delta) for BOXER mesh (a) and ICEM (b) mesh.

The combination of graphs shows that the full convergence of results is obtained at 10 M if both meshes are considered at the same time, nevertheless, the BOXER mesh reaches that convergence after 2 M cells are used. Considering that the CPU time increased by 11 hours from 2 M to 10 M cell, it could be concluded that the BOXER mesh with a total cell count of 2 M elements could be used.

An in-depth analysis of the different results from both meshing techniques, considering convergence behavior of physical quantities of interest, ensuring a convergence criteria for the residuals of at least 1E-6, and evaluating the CPU time, has been conducted to aid the selection of a meshing technique and density that would provide reliable and robust results to quantify the heat transfer performance of the original Serpentine Cold plate. For this case, the hexa-dominant mesh created in BOXER using 2 M elements has been chosen. The values presented in Table 3 will be used as Datum CFD for verification purposes when comparing the original case to the topology optimized Cold Plate performance.

TABLE 3: Summary CFD results

BOXER	2 M cells	Hex-Mesh
Y+	0.6	
ΔP (Pa)	17495.0	
	Solid Wall	Heat Cells
Min T (K)	349.5	355.6
Max T (K)	372.5	373.0
ΔT (K)	23.1	17.4
Average T (K)	364.8	363.5

2.2 The Optimized Cold Plate

The optimized cold plate is the result of a fluid topology optimization process using software from TOffeeAM. The approach used by the solver follows the algorithm described in Pietropaoli et al. [15]. The TOffeeAM platform has several modules available. In this case the electric module is used, which includes multiphysics effects for thermal heating, fluid flow and Joule heating. In this work, electrical effects are neglected; only thermal dissipation and fluid properties are specified as an input. A detailed description of the objective function optimized is shown below.

2.2.1 Fluid Topology Optimization Method

The optimization algorithm utilizes an adjoint volume of fluid approach whereby a scalar value is associated with each point in the design domain to indicate resistance to fluid flow. Physically this is interpreted as impermeability of the solid material. The optimization routine iteratively solves the computational fluid dynamics problem and updates the impermeability to satisfy the objective function subject to constraints, both of which are described in the next section. This results in an optimal distribution of solid material.

The design domain is treated as a porous flow problem with a Brinkman formulation [33] and is governed by Equations 1-3. Equation 1 is the incompressible Navier-Stokes equation with field variables for the velocity vector, $\boldsymbol{u}$, and pressure, p, and fluid properties for density, ρ, dynamic viscosity, μ, and the Brinkman penalization term where α is the scalar value for impermeability. Conservation of mass for an incompressible fluid is given by Equation 2.

$$\rho(\boldsymbol{u}\cdot\nabla)u = -\nabla p + \nabla\cdot\left(\mu(\nabla\boldsymbol{u} + \nabla^t\boldsymbol{u})\right) - \alpha\boldsymbol{u} \quad (1)$$

$$\nabla\cdot\boldsymbol{u} = 0 \quad (2)$$

The thermal energy is given by an incompressible advection-diffusion equation for energy where c is the specific heat capacity and k is the thermal conductivity and both are treated as a linear combination of the fluid and solid.

$$\rho c\boldsymbol{u}\cdot\nabla T - \nabla\cdot(k\nabla T) = 0 \quad (3)$$

2.2.2 The Optimization Objective Function

The objective function, F, is a linear combination of weighted components describing the mechanical energy of the fluid, F_1, and the total thermal energy, wF_2.

$$F = F_1 + wF_2 \quad (4)$$

$$F_1 = \int_\Gamma \left(p + \frac{1}{2}\rho\boldsymbol{u}^2\right)\boldsymbol{u}\cdot\boldsymbol{n}\,d\Gamma \quad (5)$$

Where F_1 is a scalar value related to the weighted mechanical energy component of the objective function. F_1 contains the physical terms for the fluid pressure, p, velocity, $\boldsymbol{u}$, density, ρ, and the outward facing normal, $\boldsymbol{n}$.

The objective for the thermal energy, F_2, is defined on the volume, Ω, and is formulated from the fluid temperature, T, density and heat capacity, c.

$$F_2 = \int_{\Omega} \rho c T \, d\Omega \qquad (6)$$

The weight w is used to modify the relative importance of the thermal energy term and was set to a value of 0.75 for this study. By increasing w the objective function accepts greater mechanical energy losses to increase thermal energy extraction.

The optimization problem is formulated to minimize F subject to the physical constraints, R, which are the governing equations for the design domain.

$$\begin{aligned} &minimize\ F(F_1, F_2),\ subject\ to\ R(p, \boldsymbol{u}, T) \qquad (7) \\ &R_{\boldsymbol{u}} = \rho(p + \nabla)\boldsymbol{u} + \nabla p - \nabla \cdot \left(\mu(\nabla \boldsymbol{u} + \nabla^t \boldsymbol{u})\right) + \alpha \boldsymbol{u} \\ &R_p = \nabla \cdot \boldsymbol{u} \\ &R_T = \sum_{i=f,s} [\rho c \boldsymbol{u} \cdot \nabla T - \nabla \cdot (k \nabla T)]_i \end{aligned}$$

The constraint $R_{\boldsymbol{u}}$ is the Navier-Stokes equation modified with a Brinkman penalization term, where α is the impermeability. R_p indicates the incompressibility of the Navier-Stokes equation. R_T is a convection-diffusion equation to describe the transport of thermal energy in the combined fluid, f, and solid, s, domain.

2.2.3 The Optimization Setup

To create the optimized cold plate, the solver considers a directional optimization, resulting in a two-dimensional geometry. The optimized geometry is obtained imposing several manufacturing constraints like minimum passing area, minimum features size (in the x and y direction independently). While the geometry has been developed for additive manufacturing, the part can be obtained by several manufacturing processes like milling with diffusion bonding. The solver can add filleted features and instrumentation constraints into the domain, not shown in the current design.

A single objective function was used for the entire domain with a unique weight on the temperature term for each heat source. This was to mitigate a situation where the temperature in the first source is much larger than the third source. Each heat source produced a power of 400 W to which a weighting of 0.8, 0.9 and 1.0 was applied for the first, second and third heat sources respectively.

The distribution of fluid and solid was constrained by specifying what portion of each domain would be filled with solid. These volume fractions were 40% in the diffuse region and 45% in each of the source regions.

The fluid topology optimization was run on TOffeeAM's cloud computing platform. The process used an 18 core computer and ran for nearly 20 hours. This is about 5 times than a comparable CFD simulation. The optimizer uses a *one-shot* simulation driven approach to estimate the performance of the final geometry in 2D. Subsequently, the performance in 3D is determined using the previously described CHT method with the same setup as the datum case.

For consistency, all the performances discussed in this work are based on the results obtained after with CHT analysis carried out by Rolls-Royce using the commercial solver ANSYS Fluent v19.0 and the same mesh resolution as discussed previously for the baseline and the optimized cases.

The height of the channel was kept the same as the height of the serpentine, while using the same mass flow.

3. RESULTS AND DISCUSSION

The datum and the initial optimum designs are shown in Figure 9. The serpentine design consists of a narrow reversing tube between the inlet and outlet such that the central portion of the domain is cooled. The optimized design is comprised of numerous flow channels that guide the coolant into the center of the heated regions and then out through the bottom and into an exhaust channel that leads to the outlet. There are channels formed outside of the primary heat source regions which guide cool fluid from the inlet to the far heat sources. The optimizer generated several blocking structures between the heat sources that drive fluid into the sides of the hot regions.

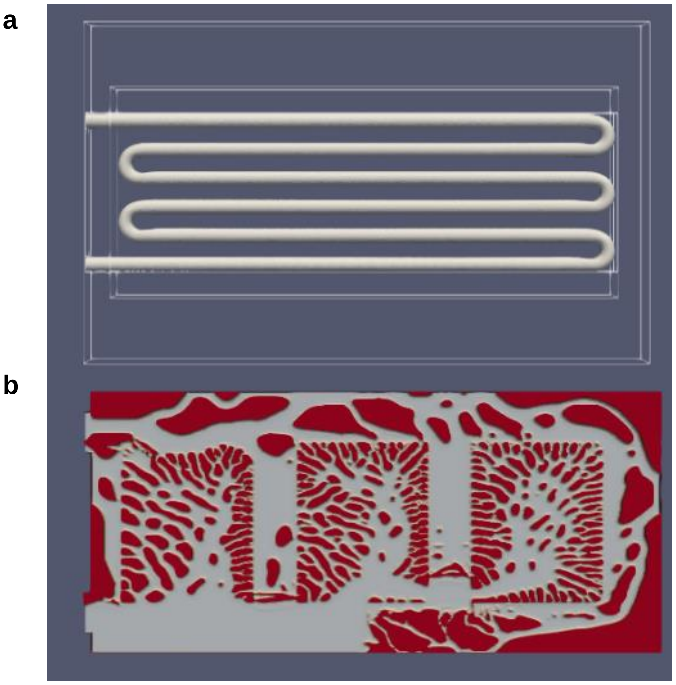

FIGURE 9: Diagrams indicated the solid and fluid regions of the serpentine design (a) and the optimized design (b).

The fluid velocities are shown in Figure 10. The serpentine design, 10a, develops an axisymmetric parabolic flow profile shortly after thin let. This profile is disrupted by the first U-bend creating a high velocity point at the top of the turn and a stagnation point at the bottom of the turn. This pair is repeated at every U-bend. At each U-bend and immediately down-steam are the regions which disturb the flow and create 3D fluid mixing within the pipe. This is the primary source of convection within the pipe. Peak fluid velocity reaches 2.7m/s. Between the U-bends the flow tends back towards an axisymmetric parabolic profile but does not fully reach this state. In contrast the velocity field in the optimized geometry is much more chaotic. At the inlet there is a fluid splitter which divides the flow into a small channel to feed the nearby heat source and, a large channel that feeds the rest of the cold plate, Figure 9b. In the small channel, the fluid velocity approaches 3m/s. In the large channel the mean fluid velocity is around 1.6m/s which makes it comparable to the inlet velocity of the serpentine.

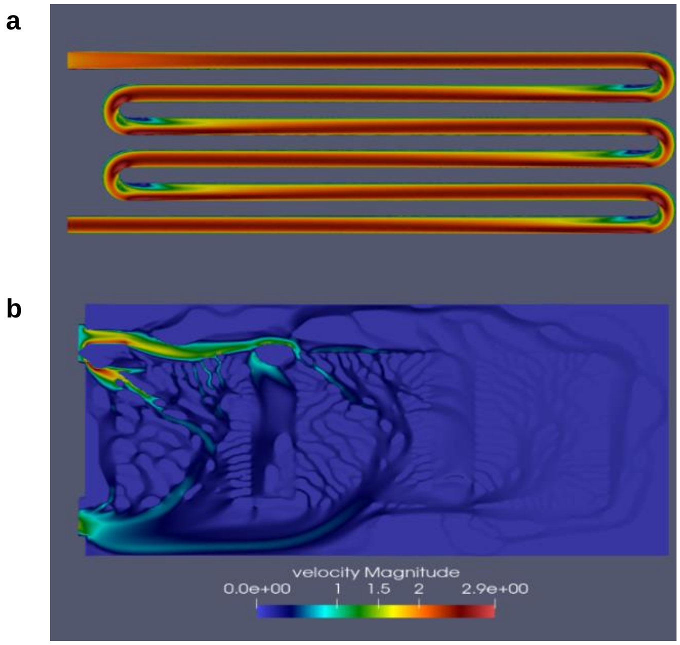

FIGURE 10: Velocity contours in m/s from the central cross-section of the serpentine design (a) and the optimized design (b).

Figure 11 shows temperature contours for a cross-section through the center of the cold plate. Both designs produce hot and cold regions but differ in their distributions. The serpentine design experiences a temperature increase from top to bottom while the optimized design has a warm region in the third cell. The peak temperatures are 394K and 390K for the serpentine and optimized designs respectively.

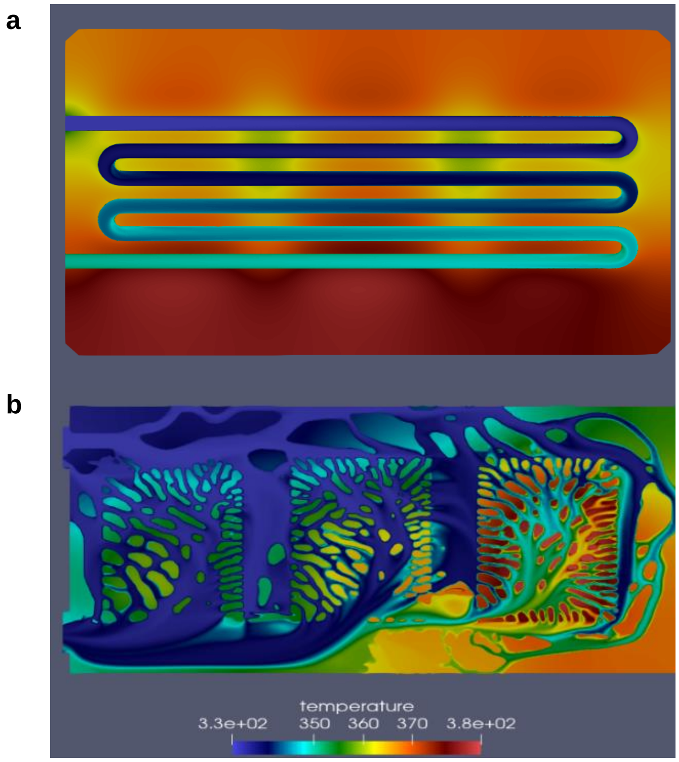

FIGURE 11: Temperature contours in degrees K from the central cross-section of the serpentine design (a) and the optimized design (b).

The heat spreader in which the heat sources are imbedded reduces local hot spots. The serpentine design has a peak temperature in the lower third region, while for the optimized design the peak is located around the third heat source. The peak temperatures are 394K and 390K for the serpentine and optimized designs respectively which means that some of the islands are the same temperature as the outer surface.

The pressure profiles are shown in Figure 12. The pressure drop from the inlet to the outlet is 17kPa for the serpentine case and 6.1kPa for the optimized case. The large pressure drop in the serpentine case is directly related to the five U-bends. This structure requires the entire mass to of fluid to turn through 180 degrees. The force required to change the fluid's momentum is supplied entirely by the pressure gradient. Whereas in the optimized case, while a streamline experiences many small turns, these sum to a little more than one U-bend. There is a static point at the inlet splitter for the optimized case that accounts for 3kPa, or about half, of the total pressure loss in the system.

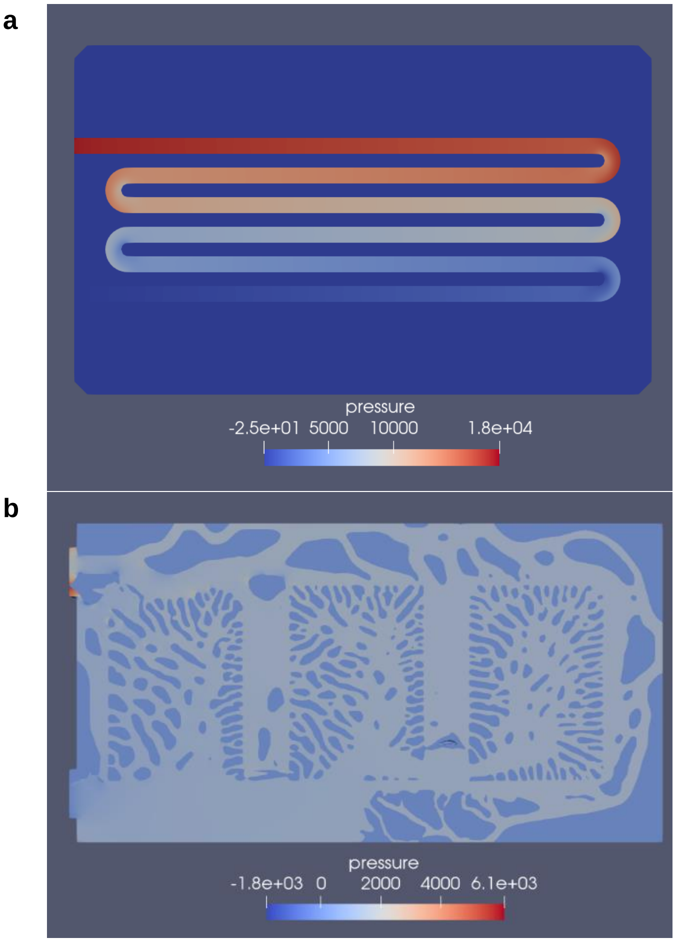

FIGURE 12: Pressure distribution in Pascals for the serpentine case, a, and in the optimized case, b. Note that the scale for the optimized case has been cropped for clarity to remove the static point at the splitter. The peak in this region was 6.1kPa and distorted the contour plot.

It is clear from Figure 11b that the fluid around the third heat source is being heated to a greater extent than in the other two sources. This is a consequence of the reduced fluid flux in that region and is a sign the objective function could be specified better either through better representation of the heat distribution or through coupling of the design space and heat spreaders. For the generic test case used here, all the heat sources produce the same power and because they are embedded in the heat spreaders, their power is partially diffused. In the 2D design space used to optimize the geometry this translates to three primary heat sources and a small source in the diffused region whose magnitude and diffusion are unknown *a priori*. This diffused region contributes some power to the fluid domain in a way that was not seen by the optimizer. This means that the large solid members on the far side of figure 10b do not contribute any heat to the objective function. Capturing this effect during the optimization would represent an important addition to this design. There are several methods available to address this with the simplest being an iterative approach where the different weightings applied to the heat sources during the optimization. However, a more robust approach would be to optimize the fluid domain in the presence of the heat spreader. This coupling would greatly improve the effectiveness of the objective function.

The reduction in pressure loss is an advantage of the current optimized design. While the primary objective of a cold plate is to remove thermal energy, it requires a pump to maintain the flow rate. A lower pressure gradient relaxes energy demands on that pump. It also means that the optimized design can operate at a higher mass flow rate while staying within pressure loss constraints. In practical applications this would translate to a lower temperature throughout.

Since the pressure difference is so large between the two designs it suggests that the objective function could be more heavily weighted towards the thermal term.

A prime concern with topology optimized designs is their manufacturability. Here, where the optimized design was extruded from 2D, there are at least two possible options; milling and additive manufacture. Both require a minimum feature length, which was specified here as 0.5mm for the solid part. In the milling scenario, material is removed by means of a rotating cutter. The minimum feature is actually defined on the fluid channel width and is dependent on the cutter available. In the additive case the minimum feature is defined on the solid material. Additive techniques are further constrained by overhanging material between layers. Here, this has been addressed by applying self supporting rules for the channels, not shown in the current papers.

The two designs inherently have a different mass. The serpentine pipe occupies 19.5% of the design space while the remainder, 79.5%, is solid aluminum. Due to the optimized design's volume fractions (40% in the diffused region and 45% in the heat sources) its solid content is about 42% aluminum. This is a 38.5% decrease of the solid mass in the design space.

For the case presented here the optimized design offers improvements over the serpentine case for reducing peak temperature and reducing pressure losses. Though an often-desired case is a heat exchanger where the heat distribution is uniform. This scenario prevents hot spots and reduces thermal stresses across the component. Though this was not specified in the objective function it represents an industrially useful addition.

A significant advantage of the optimized design is its design process. It is created by defining the problem space and the manufacturing constraints. The case presented here has a relatively simple geometry. In situations facing the next generation of aircraft, designers can use fluid topology optimization to address more spatially constrained cooling scenarios. Fluid topology optimization requires only the design space and location of the heat sources to create efficient cooling solutions. The complexity of the design process does not increase with complexity of the design domain.

4. CONCLUSION

This article presents a comparative study between a traditional serpentine cold plate, and one designed by the fluid Topology Optimization solver TOffee (from TOffeeAM) that is focused on thermal management of electric components. The two designs contain vastly differing flow paths where the Toffee optimizer built microchannels able to efficiently cool the plate.

The comparison of the performances of the two geometries has been carried out using commercial solvers and two mesh generators. The optimized design has a lower peak temperature but very high cooling near the inlet region. Fluid topology optimized designs offer a promising route forward for creating efficient cold plates.

By minimizing the number of U-bends, the pressure drop of the geometry optimized by TOffeeAM has 65% lower pressure drop than in the serpentine. The maximum temperature is 4 degrees lower and a 38.5% reduction in the mass of the solid design space.

ACKNOWLEDGEMENTS

The authors would like to acknowledge Rolls-Royce for the permission to publish this work. The authors would like to acknowledge and thank Mr Pete Smith (RR Thermo-Fluid Systems) for providing the datum heat-exchanger test case, our PhD researcher Mario Carta (RR Future Methods) for the BoXer meshing support and Dr Indi Tristanto for many useful discussions and support of the Ansys fluent simulations.

TOffeeAM granted Rolls-Royce access to the TOffeeAM design platform under the grant PO: GB-PO-279044.

References

[1] A. Bills, S. Sripad, W. Fredericks, M. Singh and V. Viswanathan, "Performance metrics required of next-generation batteries to electrify commercial aircraft," *ACS Energy Letters,* pp. 663-668, 2020.

[2] J. Hayes, K. George, P. Killeen, B. McPherson, K. Olejniczak and T. McNutt, "Bidirectional, SiC module-based solid-state circuit breakers for 270 V dc MEA/AEA systems," *IEEE 4th Workshop on Wide Bandgap Power Devices and Applications (WiPDA),* pp. 70-77, 2016.

[3] R. Falck, J. Chin, S. Schnulo, J. Burt and J. Gray, "Trajectory optimization of electric aircraft subject to subsystem thermal constraints," *18th AIAA/ISSMO Multidisciplinary Analysis and Optimization Conference,* p. 4002, 2017.

[4] S. Jafari and T. Nikolaidis, "Thermal management systems for civil aircraft engines: Review, challenges and exploring the future," *Applied Sciences,* p. 2044, 2018.

[5] B. Brelje and J. Martins, "Electric, hybrid, and turboelectric fixed-wing aircraft: A review of concepts, models, and design approaches," *Progress in Aerospace Sciences,* pp. 1-19, 2019.

[6] M. Turkyilmazoglu, " Efficiency of heat and mass transfer in fully wet porous fins: exponential fins versus straight fins," *International journal of refrigeration,* pp. 158-164, 2014.

[7] L. Lu, X. Han, J. Li, J. Hua and M. Ouyang, "A review on the key issues for lithium-ion battery management in electric vehicles," *Journal of power sources,* pp. 272-288, 2013.

[8] S. Coşkun and M. Atay, "Fin efficiency analysis of convective straight fins with temperature dependent thermal conductivity using variation iteration method," *Applied Thermal Engineering,* pp. 2345-2352, 2008.

[9] S. Liu, Y. Huang and J. Wang, "Theoretical and numerical investigation on the fin effectiveness and the fin efficiency of printed circuit heat exchanger with straight channels," *International Journal of Thermal Sciences,* pp. 558-566, 2018.

[10] I. Kaur and P. Singh, "State-of-the-art in heat exchanger additive manufacturing," *International Journal of Heat and Mass Transfer,* p. 121600, 2021.

[11] P. He, C. Mader, J. Martins and K. Maki, "Aerothermal optimization of a ribbed U-bend cooling channel using the adjoint method," *International Journal of Heat and Mass Transfer,* 2019.

[12] T. Deng, G. Zhang and Y. Ran, "Study on thermal management of rectangular Li-ion battery with serpentine-channel cold plate," *International Journal of Heat and Mass Transfer,* pp. 143-152, 2018.

[13] C. Mangrulkar, A. Dhoble, S. Chamoli, A. Gupta and V. Gawande, "Recent advancement in heat transfer and fluid flow characteristics in cross flow heat exchangers," *Renewable and Sustainable Energy Reviews,* p. 109220, 2019.

[14] L. Høghøj, D. Nørhave, J. Alexandersen, O. Sigmund and C. Andreasen, "Topology optimization of two fluid heat exchangers," *International Journal of Heat and Mass Transfer,* p. 120543, 2020.

[15] M. Pietropaoli, F. Montomoli and A. Gaymann, "Three-dimensional fluid topology optimization for heat transfer," *Structural and Multidisciplinary Optimization,* pp. 801-812, 2019.

[16] S. Kambampati, J. Gray and H. Kim, "Level set topology optimization of load carrying battery packs," *International Journal of Heat and Mass Transfer,* p. 121570, 2021.

[17] X. Mo, H. Zhi, Y. Xiao, H. Hua and L. He, "Topology optimization of cooling plates for battery thermal

management," *International Journal of Heat and Mass Transfer,* 2021.

[18] M. Tomlin and J. Meyer, "Topology optimization of an additive layer manufactured (ALM) aerospace part," *Proceeding of the 7th Altair CAE technology conference ,* pp. 1-9, 2011.

[19] L. Berrocal, R. Fernández, S. González, A. Periñán, S. Tudela, J. Vilanova, L. Rubio, J. Márquez, J. Guerrero and F. Lasagni, "Topology optimization and additive manufacturing for aerospace components," *Progress in Additive Manufacturing,* pp. 83-95, 2019.

[20] R. Murphy, C. Imediegwu, R. Hewson and M. Santer, "Multiscale structural optimization with concurrent coupling between scales," *Structural and Multidisciplinary Optimization,* pp. 1721-1741, 2021.

[21] T. Dbouk, "A review about the engineering design of optimal heat transfer systems using topology optimization," *Applied Thermal Engineering,* vol. 112, pp. 841-854, 2017.

[22] K. Chen, Y. Chen, M. Song and S. Wang, "Multi-parameter structure design of parallel mini-channel cold plate for battery thermal management," *International Journal of Energy Research,* pp. 4321-4334, 2020.

[23] X. Xu, G. Tong and R. Li, ". Numerical study and optimizing on cold plate splitter for lithium battery thermal management system," *Applied Thermal Engineering,* p. 114787, 2020.

[24] B. Blakey-Milner, P. Gradl, G. Snedden, M. Brooks, J. Pitot, E. Lopez, M. Leary, F. Berto and A. du Plessis, "Metal additive manufacturing in aerospace: A review," *Materials & Design,* p. 110008, 2021.

[25] D. Jafari and W. Wits, "The utilization of selective laser melting technology on heat transfer devices for thermal energy conversion applications: A review," *Renewable and Sustainable Energy Reviews,* pp. 420-442, 2018.

[26] J. Liu, A. Gaynor, S. Chen, Z. Kang, K. Suresh, A. Takezawa, L. Li, J. Kato, J. Tang, C. Wang and L. Cheng, "Current and future trends in topology optimization for additive manufacturing," *Structural and Multidisciplinary Optimization,* pp. 2457-2483, 2018.

[27] C. Babu, P. Kumar, S. Roy and D. Kanungo, "CFD analysis of an economizer for heat transfer enhancement using serrated finned tube equipped with variable fin segments," *Materials Today: Proceedings,* pp. 222-230, 2021.

[28] C. Sinn, G. Pesch, J. Thöming and L. Kiewidt, "Coupled conjugate heat transfer and heat production in open-cell ceramic foams investigated using CFD," *International Journal of Heat and Mass Transfer,* pp. 600-612, 2019.

[29] A. Papukchiev, D. Grishchenko and P. Kudinov, "On the need for conjugate heat transfer modelling in transient CFD simulations," *Nuclear Engineering and Design,* p. 110796, 2020.

[30] S. Patankar and D. Spalding, "A calculation procedure for heat, mass and momentum transfer in three-dimensional parabolic flows," *Nermerical prediction of flow, heat transfer, turbulence and combustion,* pp. 54-73, 1983.

[31] "ANSYS Fluent User's Guide," ANSYS, Inc., 2019.

[32] A. Demargne, R. Evans, P. Tiller and W. Dawes, "Practical and reliable mesh generation for complex, real-world geometries," *52nd Aerospace Sciences Meeting,* p. 0119, 2014.

[33] H. Brinkman, "A Calculation of the Viscous Force Exerted by a Flowing Fluid on a Dense Swarm of Particle," *Flow, Turbulence and Combustion,* pp. 27-34, 1949.